IEEE Access
Multidisciplinary ⋮ Rapid Review ⋮ Open Access Journal

Received 22 February 2023, accepted 24 March 2023, date of publication 31 March 2023, date of current version 5 April 2023.

Digital Object Identifier 10.1109/ACCESS.2023.3263486

RESEARCH ARTICLE

High Efficiency LLC Resonant Converter With Wide Output Range of 200–1000 V for DC-Connected EVs Ultra-Fast Charging Stations

AHMED ELEZAB[1], (Student Member, IEEE), OMAR ZAYED[1], (Graduate Student Member, IEEE), AHMED ABUELNAGA[2], (Member, IEEE), AND MEHDI NARIMANI[1], (Senior Member, IEEE)

[1]Electrical and Computer Engineering, McMaster University, Hamilton, ON L8S 4K1, Canada
[2]Rockwell Automation, Cambridge, ON N1R 5N9, Canada

Corresponding author: Ahmed Elezab (elezaa1@mcmaster.ca)

ABSTRACT DC-connected ultra-fast chargers consist of isolated DC/DC converter modules to provide the required charging profile. This paper proposes a charging module that interfaces with a fixed voltage DC-bus and covers a wide variety of electric vehicles (EVs) with battery voltages ranging from 200 to 1000 V. DC/DC converters for EVs charging has been discussed several times in the literature, however the DC-connected structure with fixed DC-bus voltage is rarely considered. This paper proposes a full-bridge LLC DC/DC converter module with a configurable secondary. This configuration extends the converter's charging voltage range without adding stress on the resonant components or operating far from the unity gain point. Due to wide output range, the converter parameters are optimized using the time-domain analytical model to cover the required range without adding unnecessary circulating current that compromises the efficiency. First, the LLC resonant converter fundamentals are briefly introduced. Then, the proposed topology operation and advantages are discussed. After which, the converter's requirements and design method are presented, focusing on circulating current minimization. Finally, the effectiveness of the proposed converter and the optimized design strategy is verified experimentally on a 10 kW prototype with an input of 800 V and an output of 200 - 1000 V.

INDEX TERMS LLC resonant converter, dc/dc converters, electric vehicle fast charging, reconfigurable structure, wide output range.

I. INTRODUCTION

Transportation electrification has received huge attention recently due to its potential to mitigate the energy sustainability problems and the environment crises [1]. However, the long charging time and the limited range per charge are challenging the growth of the electric vehicles market. Fast charging helps reducing the charging time. Hence, it is a major necessity for the transportation electrification adoption [2], [3], [4].

The associate editor coordinating the review of this manuscript and approving it for publication was Vitor Monteiro.

The typical electric car battery voltage is around 400 V. However, the next generation of EVs such as Auston Martin and Porsche are developing EVs with 800 V battery systems, to increase the charging power without increasing the charging current and losses [5]. Therefore, the charging stations are required to cover the voltage range of 200-1000 V that covers the typical and future electric car batteries [6], [7].

DC-Connected EVs fast charging station systems are still not widely adopted due to unmature standards and protection coordination. However, transferring the power using fixed dc voltage provides several advantages regarding its compatibility with renewable energy sources, size, efficiency and cost

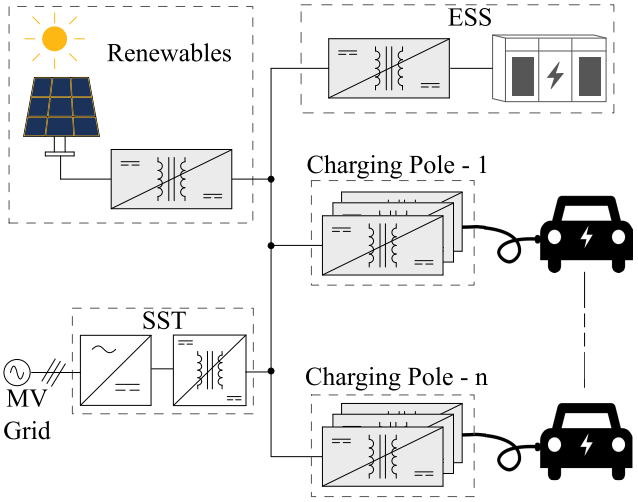

FIGURE 1. DC-connected fast charging station.

when compared to the ac-connected charging systems [2]. The charging module in dc-connected fast charging station needs to cover a wide output voltage range of 200-1000 V. Moreover, the charging station should have a flexible structure to facilitate charging at higher power levels. So, the charging module should be easily stacked to increase charging power.

Several solutions have been proposed in the literature for the ultra-fast chargers, however most of them are for ac-connected structures assuming variable input voltage to the charging module [6], [8], [9], [10], [11]. Nevertheless, some researches proposed solutions for dc-connected structures. In [12] and [13], the authors proposed a solution with partial power processing, reducing the converter losses by processing only a fraction of the power transferred to the vehicle. However, this approach does not ensure galvanic isolation between the station dc-bus and the vehicles. Another approach in [14], the authors proposed a three-port converter with one input port, and two output ports. One output port is for slow charging and the other output port is for fast charging. The proposed three-port converter showed promising reduction in the volume, cost, and control complexity, while operating at high efficiency. However, only limited output voltage range of 200-400 V is considered. Covering the wide range of 200-1000 V is challenging in dc-connected fast chargers. One solution is a cascaded connection of two converters, an isolated converter for achieving galvanic isolation. Then, followed by another converter which provides the required charging voltage and current. This approach fixes the isolated converter gain at one, achieving high operating efficiency over the charging range. However, it adds another non-isolated converter, increasing the number of components and total cost. Moreover, the achieved voltage range is limited [15].

Phase-shift Dual-Active bridge (PS-DAB) converters and LLC resonant converters have been widely utilized as the dc/dc converter for EV fast chargers [14], [15], [16], [17], [18], [19]. For wide voltage range applications, LLC has gained more attention lately due to zero voltage-switching (ZVS), low electromagnetic interference (EMI), and high-efficiency operation [15], [16], [20], [21]. LLC resonant converter has been widely used for EVs DC fast charging [2], [5], [22], [23]. However, it still suffers from high circulating current causing high conduction losses, and a wide frequency range causing complex design. Several solutions for general wide voltage range applications have been proposed to solve these drawbacks. Hybrid control between Phase Shift Modulation (PSM) and Frequency Modulation (FM) is used to reach a wide voltage range [24], [25]. However, it requires complex analysis to ensure ZVS operation for the lagging leg at light load. Topology reconfiguration solutions are presented for wide output range applications; however, limited voltage range and power level is achieved [21], [26], [27].

In this paper, a high efficiency solution for a universal output range DC fast charging module is presented. A configurable secondary LLC resonant converter is proposed to extend the output range of the converter without adding burden on the resonant tank. To ensure high performance charging, the converter resonant components are optimized for the common EVs charging profiles. FHA does not have acceptable accuracy when used for wide voltage range design [28]. Therefore, the LLC resonant converter time-domain analytical model is used to find the optimized resonant components values to achieve just the required output voltage range without unnecessarily wider range increasing the converter circulating current and compromising the efficiency.

This paper is organized as follows; Section II presents the proposed topology and its operation principle. In section III, the design process of the converter is presented. In section IV, the experimental results are provided and compared with the literature to verify the effectiveness of the proposed topology. Finally, the conclusion is provided in Section V.

II. PROPOSED TOPOLOGY OPERATION

In this section, the proposed topology operation principle and advantages are presented. Fig.2 shows schematic of the proposed converter. The proposed topology has an input voltage V_{in}, full-bridge switches S_1, S_2, S_3, S_4, resonant inductor L_r, then the resonant capacitor is split into two $C_r/2$, and two gapped transformers T_{r1}, and T_{r2}. Each with magnetizing inductance $2L_m$, where L_m is the required magnetizing inductance. The transformer is designed to have a low leakage inductance to be neglected during the design process. On the secondary-side, there are two diode full-bridge rectifiers and three contactors that connect the secondaries in parallel or in series configurations. In parallel mode (PM), the contactors S_{p1} and S_{p2} are closed and S_s is open. In series mode (SM) the contactor S_s is closed, while S_{p1} and S_{p2} are open.

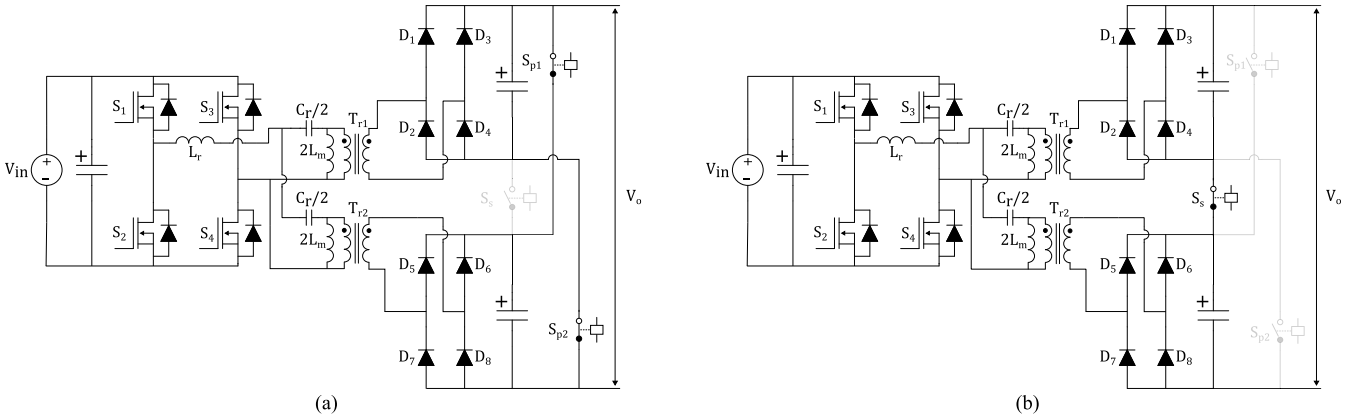

FIGURE 2. Proposed Topology (a) Parallel Mode (PM) (b) Series Mode (SM).

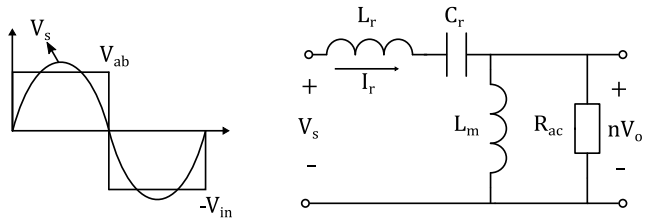

FIGURE 3. FHA equivalent model of an LLC resonant converter.

A. CONVENTIONAL LLC RESONANT CONVERTER OPERATION PRINCIPLE

The LLC resonant converter operation is typically analyzed using the First Harmonic Approximation (FHA). Fig. 3 shows the equivalent FHA model of the LLC resonant converter. V_s is the first harmonic component of the H-bridge output to the resonant tank V_{ab}. The resonant tank has two resonant frequencies f_r and f_m and can be defined as:

$$f_r = \frac{1}{2\pi\sqrt{L_r \cdot C_r}} \tag{1}$$

$$f_m = \frac{1}{2\pi\sqrt{(L_r + L_m) \cdot C_r}} \tag{2}$$

The converter switching frequency (f_{sw}) must be higher than f_m, to operate in the inductive region, where the current lags the voltage, so that ZVS is achieved. The conversion gain ratio of the converter can be calculated as:

$$M_g = \frac{L_n f_n^2}{\left[(1+L_n)f_n^2 - 1\right] + j\left[\left(f_n^2 - 1\right) f_n Q_e L_n\right]} \tag{3}$$

where L_n is the inductance ratio and can calculated by

$$L_n = L_m / L_r \tag{4}$$

Q_e is quality factor and can be represented by:

$$Q_e = \sqrt{\frac{L_r}{C_r}} / R_{ac} \tag{5}$$

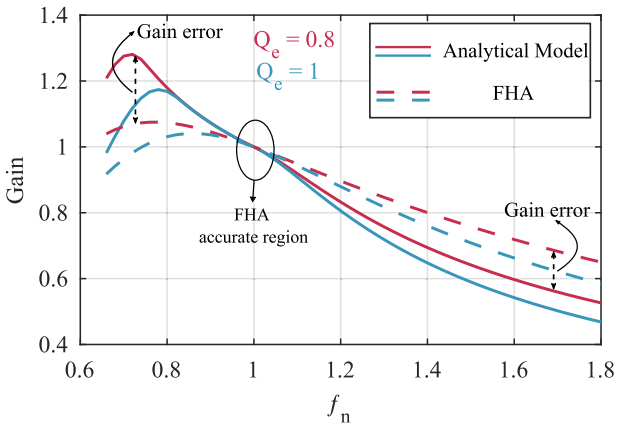

FIGURE 4. FHA gain curve versus steady state analytical model gain curve.

f_n is the normalized switching frequency to the resonant frequency f_r, and can be defined as:

$$f_n = f_{sw} / f_r \tag{6}$$

where f_{sw} is the converter switching frequency.

In section III, the effect of Q_e, L_n is presented in detail to show their effect on the converter performance.

FHA has poor accuracy when applied at frequencies far from the resonant frequency. Fig. 4 shows the FHA gain against the actual gain obtained from the time-domain analysis. It can be seen that the FHA underestimates the gain performance of the converter, leading to converter parameters that provide unnecessarily wider voltage range. However, it causes additional circulating current and conduction losses. Therefore, a more accurate approach using a time-domain analytical model is developed to determine the converter parameters to reach the voltage and power range.

In the LLC resonant converter analytical model, there are three equivalent circuits at the positive half-cycle and three equivalent circuits at the negative half-cycle. Since the converter waveforms are symmetrical, only the positive half-cycle equivalent circuits shown in Fig. 5 can be studied.

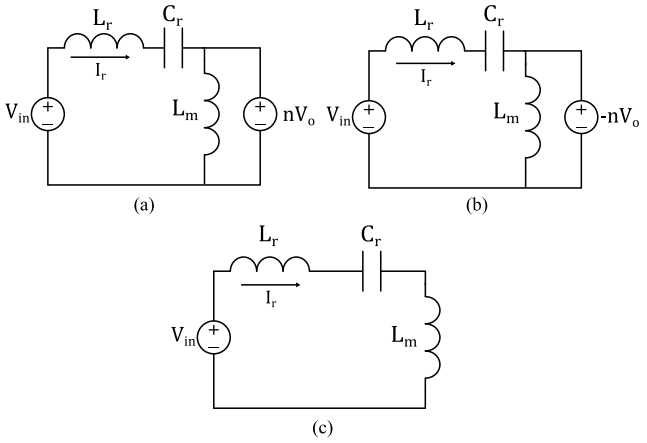

FIGURE 5. LLC Converter equivalent circuits (a) State A (b) State B (c) State C.

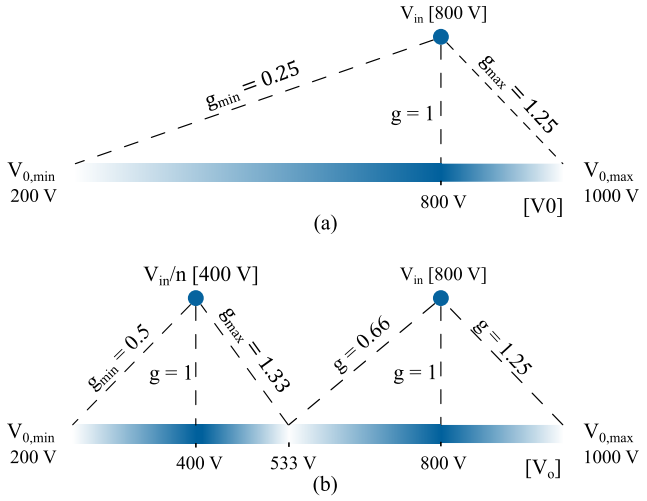

FIGURE 6. Converter resonant tank gain (a) Conventional converter (b) Proposed reconfigurable secondary converter.

At state A (shown in Fig. 5.a), the transformer reflected voltage is clamped to the positive output voltage. At state B (shown in Fig. 5.b), the reflected voltage on the primary-side is clamped to the negative output voltage. The diodes are all switched off on state C (shown in Fig. 5.c), therefore the converter primary-side is isolated from the output voltage. Each state has it own state equations. At each output voltage and load, the converter operates at different modes formed by different sequences of the three states. The steady state model solution can be achieved by considering the constrains of each operating mode then solving the steady-state equations together numerically. The time-domain analytical model is analyzed in detail in [28].

B. PROPOSED TOPOLOGY ADVANTAGES AND OPERATION

The proposed topology shown in Fig. 2, achieves double the output voltage range compared to the conventional topology by switching between the series mode (SM) and parallel mode (PM). The converter operates at PM for low output voltages, and at SM for high output voltages. This topology adds another unity gain point, allowing the converter to operate in the vicinity of the resonant frequency, limiting the efficiency drop over the wide gain range.

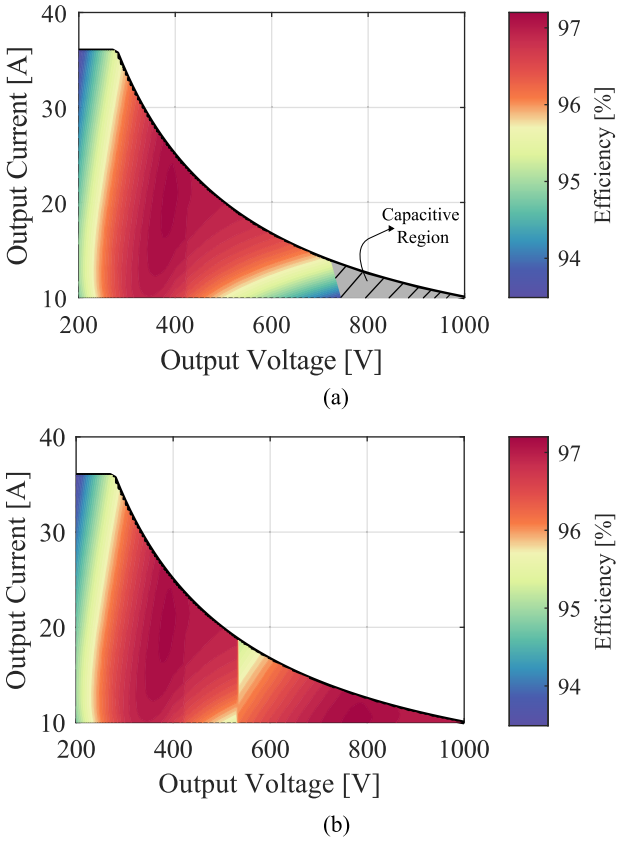

FIGURE 7. Efficiency map for 10 kW LLC resonant converter (a) conventional topology (b) Proposed topology.

Fig. 6 illustrates the resonant tank gain (g) range for the proposed topology against the conventional topology, where g can be defined as:

$$g = \frac{nV_o}{V_{in}} \tag{7}$$

Moreover, this topology reflects the same load on the primary-side resonant tank during the two secondary configurations (SM and PM) allowing the converter to operate at the same conditions (Q_e and f_n). By reducing the converter gain and load ranges, the resonant tank parameters design is drastically simplified. Additionally, the circulating current in the primary current is reduced, increasing the efficiency and allowing the usage of lower current ratings primary-side switches, resonant components, and a smaller transformer. Additionally, each rectifier is only subjected to half the output voltage, which reduces the secondary side devices voltage rating. It is also worth mentioning that this topology modularity allows fully utilization of all the components at the two modes.

To demonstrate the benefits of the proposed topology, time-domain analytical model is utilized to compare its

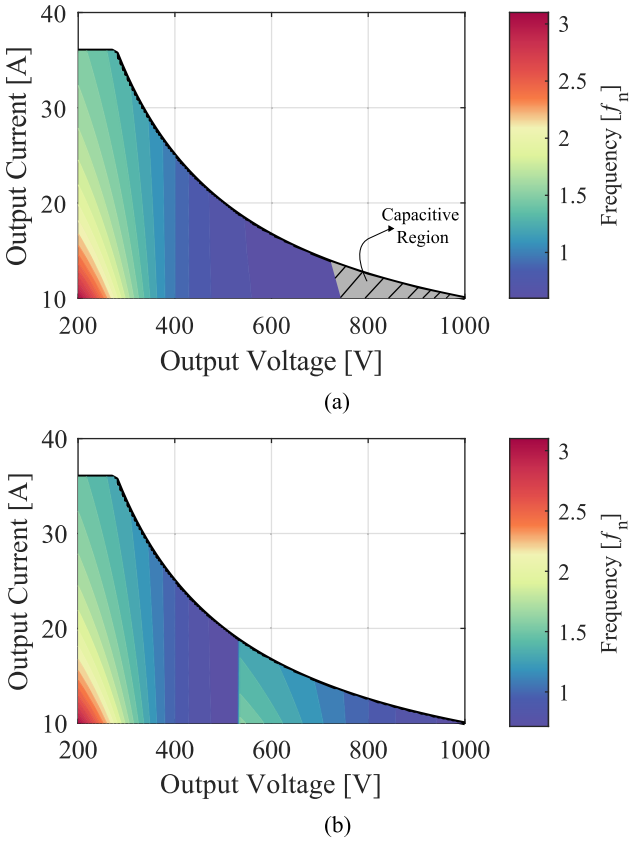

FIGURE 8. Frequency map [f_n] for 10 kW LLC resonant converter (a) conventional topology (b) Proposed topology.

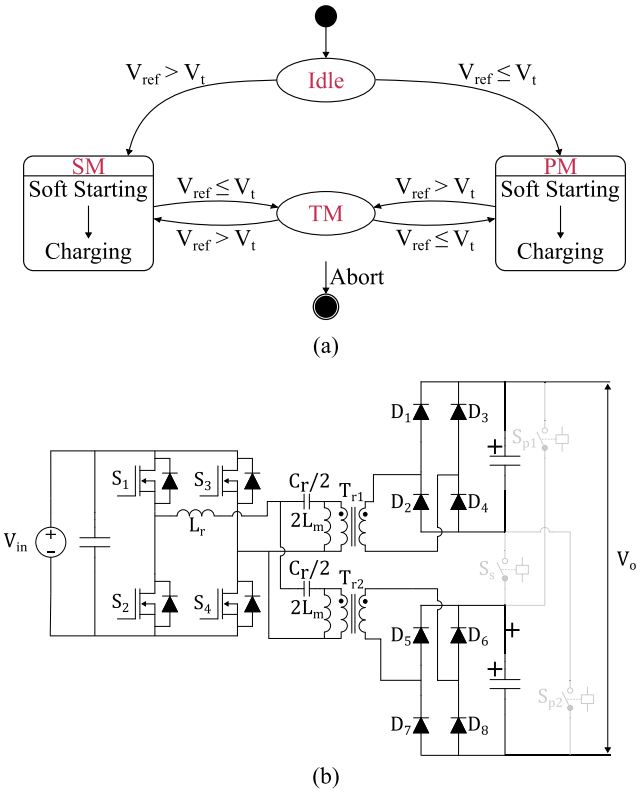

FIGURE 9. Converter mode transition scheme (a) Converter modes state diagram (b)Transition mode (TM).

performance in terms of frequency range, voltage range and efficiency with that of the conventional LLC resonant topology. A comparison between the two topologies is performed with identical converter parameters (L_r, C_r, L_m, and n). The efficiency map of the converters is presented in Fig. 7, and it shows that the proposed converter has a wider output range compared to the conventional converter. While both converters have a peak efficiency of 97.2 % based on analytical loss analysis, the proposed converter maintains high efficiency across most of the converter output range. Fig. 8 displays the frequency range of each converter, and it indicates that the conventional topology has a voltage range of [200 - 740] V and a frequency range of [0.6·f_r - 3·f_r], whereas the proposed topology has the entire required voltage range of [200 - 1000] V and frequency range of [0.7·f_r - 3·f_r].

The two main modes of operation are the parallel mode (PM) and the series mode (SM). The operation mode is selected based on the demanded output charging voltage. As will be discussed in detail later in section III, the demanded output charging voltage is compared with the determined transition voltage ($V_{transition}$). In case the demanded output charging voltage is less than $V_{transition}$, PM is selected. In the other case, SM is selected. In addition to these two modes, the transition mode (TM) is introduced, which assists the transition between PM and SM during the operation of the charger. The three states diagram is shown in Fig.9.a. At the TM, the contactors S_{p1}, S_{p2}, and S_s are turned off. The equivalent circuit of TM is shown in Fig.9.b. After transition to the operating mode (PM or SM), the LLC resonant converter starts operation to regulate the output for the demanded charging voltage and current. It should be noticed that soft starting strategy has to be implemented to reach the demanded charging voltage before charging the vehicle to avoid in rush current. Soft starting strategies is not in the scope of this work and has been discussed in detail in [29].

C. PARALLEL MODE CURRENT SHARING

The proposed topology configuration ensures that the two secondary outputs in PM are subject to equal current sharing. This is achieved by dividing the resonant capacitor (C_r) among the two transformers. By introducing the resonant capacitor (C_r) impedance in each path, the impact of parasitic impedances in the two secondaries can be disregarded in comparison to the impedance of the split resonant capacitance. This results in a balanced current distribution between the two secondaries. The current sharing can be done by splitting the resonant capacitor or the resonant inductor. It is important to note that the act of paralleling capacitors adds their capacitance value. Thus, only half of the resonant capacitance (C_r) is needed in each path. However, inductance value decreases when inductors are paralleled, meaning

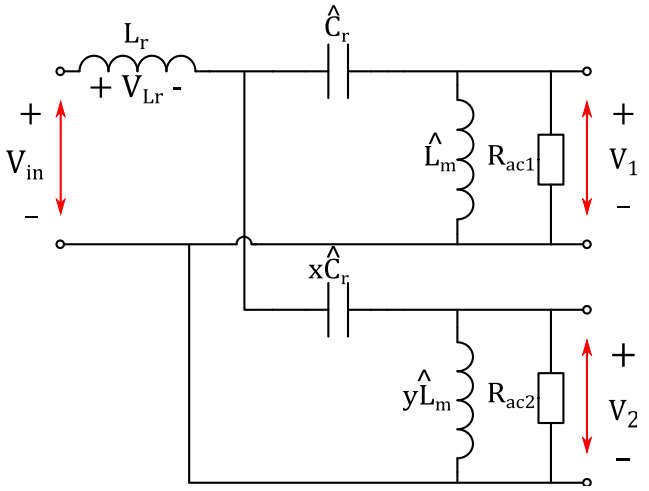

FIGURE 10. FHA equivalent circuit of the proposed topology.

that twice the resonant inductance (L_r) is required in each path. Additionally, utilizing ceramic capacitors enables the design to attain a high-power density while keeping costs low. Therefore, splitting the resonant capacitors is selected as it achieves equal current sharing and less components footprint hence higher power density. To ensure equal current sharing between the output rectifiers in PM, simple FHA analysis is carried out to model the current sharing aspect [30]. It is worthy to mention that FHA is only used for the power-sharing analysis; however, the design process and performance are analyzed by the more accurate LLC analytical model.

Fig. 10 shows the FHA equivalent circuit of the proposed topology in PM. L_r and V_{lr} are the common resonant inductor and the voltage across it, respectively. $\hat{C_r}$ and $\hat{L_m}$ are half the required resonant capacitor and double the required magnetizing inductance, respectively. At the same time, $x\hat{C_r}$ and $y\hat{L_m}$ are the resonant components in the second parallel branch, where x and y are the tolerances between the two parallel branches. At steady state, the output load equivalent resistance R_o is split into resistances (R_{o1}, R_{o2}) at each output rectifier. Hence, the reflected resistances can be split into (R_{ac1}, R_{ac2}) and defined as the following:

$$\begin{cases} R_{o1} = \dfrac{1}{k}R_o, R_{o2} = \dfrac{1}{1-k}R_0, \quad k \in [0,1] \\ R_{ac} = \dfrac{8n^2}{\pi^2}R_o, R_{ac1} = \dfrac{8n^2}{\pi^2}R_{o1}, R_{ac2} = \dfrac{8n^2}{\pi^2}R_{o2} \\ R_{ac1} = \dfrac{1}{k}R_{ac}, R_{ac2} = \dfrac{1}{1-k}R_{ac} \end{cases} \tag{8}$$

where k is the load resistance sharing error between the two secondaries. $k = 0.5$ represents the ideal case where the two rectifiers share the current equally. While $k = 0$ or $k = 1$, indicates that only one rectifier supplies the load current.

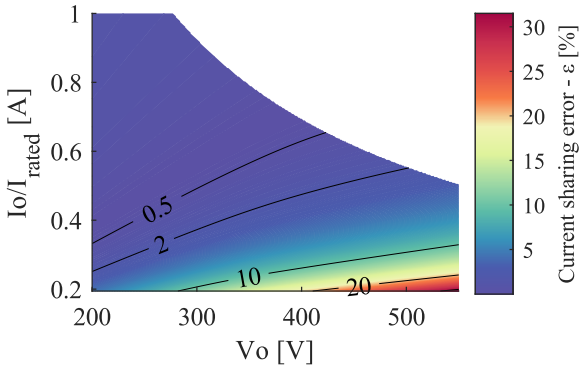

FIGURE 11. Current sharing error (ε) in PM at 3% components tolerance.

Based on Fig. 4 the voltages V_1 and V_2 can be defined as follows:

$$\begin{cases} V_1(s) = \dfrac{R_{ac1}//s\hat{L_m}}{R_{ac1}//s\hat{L_m} + 1/s\hat{C_r}}\,(V_{in}(s) + V_{Lr}(s)) \\ V_2(s) = \dfrac{R_{ac2}//sy\hat{L_m}}{R_{ac2}//sy\hat{L_m} + 1/sx\hat{C_r}}\,(V_{in}(s) + V_{Lr}(s)) \end{cases} \tag{9}$$

At PM, the two rectifiers are connected in parallel; therefore, $V_1(s)$ and $V_2(s)$ magnitude values are identical

$$|V_1(s)| = |V_2(s)| \tag{10}$$

From (8), (9), and (10), k in terms of the system parameters and the tolerances is expressed in (11), as shown at the bottom of the next page, where ω is the angular frequency. Then, the current sharing error can be determined as:

$$\varepsilon = |\frac{I_1 - I_2}{I_{load}}| = |2k - 1| \tag{12}$$

Fig. 11 shows the output current sharing error between the two secondaries. The current sharing is analyzed over the converter output current range in PM with 3 % parameter error. It can be seen that ε has its peak at low current ratings, then it starts decreasing by increasing the load, reaching less than 5 % at half the rated load.

III. DESIGN AND PERFORMANCE ANALYSIS

LLC resonant converter exhibits high efficiency and low EMI at frequencies around the resonant frequency. The three resonant components (L_r, C_r, L_m) are the essential factors to control the gain coverage and the converter performance. These three components can be represented by only two variables: the quality factor (Q_e), and the inductance ratio (L_n) even at different resonant frequency and different load. These two variables determine the performance of the converter in regards of voltage gain, components stress and converter efficiency [31]. As will be shown in this section, unnecessary extension of the voltage coverage region will compromise the converter efficiency. Therefore, in this section

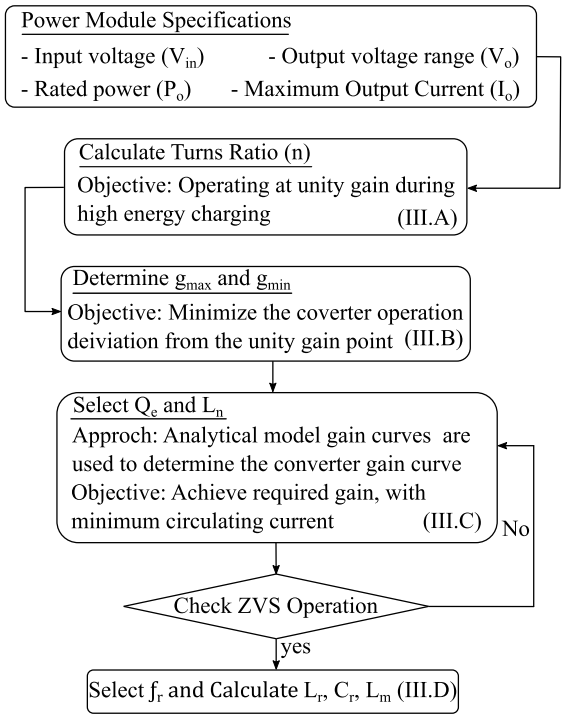

FIGURE 12. Converter design process.

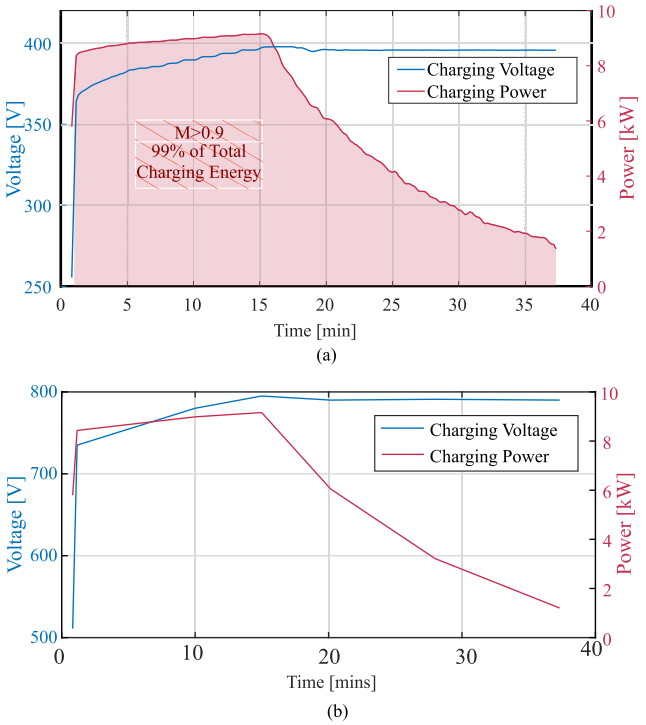

FIGURE 13. Charging profile (per 10 kW module) (a) Nissan Leaf (b) Generic 800V charging profile.

the optimal turns ratio (n), quality factor (Q_e) and inductance ratio(L_n) will be selected to cover the required voltage range without an unnecessary increase in the circulating current.

The converter design steps are shown in Fig.12. First, the converter specifications are determined. The output voltage range covers the typical electric car charging profile, in addition to higher voltage electric cars, electric buses, and electric trucks. Then, the power rating and the input voltage are selected. The converter input voltage has a limit of 1500 V to comply with the IEC 61851 standard [32]. The input voltage is selected at 800 V to enable the usage of 1200 V SiC devices. Next, the transformer turns ratio (n) is selected to set the converter output voltage around the typical electric car battery nominal voltage at the resonant tank unity-gain operation. Hence, the converter operates around the resonance frequency with minimal losses during high power charging of the typical electric vehicles. Afterwards, the converter's maximum and minimum gain can be acquired. Next, the analytical model is used to determine the quality factor (Q_e) at the rated load and the (L_n) needed to cover the required output range. Then, the resonant frequency is selected, and the resonant components values are calculated. In this section, each design step is explained in detail.

A. CALCULATE TURNS RATIO (n)

The typical electric car battery voltage is around 400 V. Nevertheless, other EVs manufacturers, electric busses, and trucks have 800 V battery systems. A generic 800 V battery charging profile is used in this work by doubling the typical 400 V battery charging profile voltage, while keeping the same charging power. Fig. 13 shows a charging profile for a typical EV (Nissan Leaf- 400V) [33] and the generic 800 V charging profile used in this paper. It can be seen in Fig. 13.a that 99 % of the charging energy is delivered to the battery at charging voltage in the vicinity of the battery nominal

$$k = \begin{cases} -\dfrac{R_{ac}^2\left(x^2y^2-1\right)-\hat{L_m}^2y^2\omega^2+2\hat{C_r}\hat{L_m}R_{ac}^2\omega^2\left(xy-x^2y^2\right)}{2\hat{L_m}^2y^2\omega^2}, & x=1 \\ \pm\dfrac{2\sqrt{\hat{L_m}^4y^4\omega^4-\hat{L_m}^2y^2\omega^2\left(x^2-1\right)\left(R_{ac}^2\left(x^2y^2-1\right)-\hat{L_m}^2y^2\omega^2+2\hat{C_r}\hat{L_m}R_{ac}^2\omega^2\left(xy-x^2y^2\right)\right)}+2\hat{L_m}^2y^2\omega^2}{2\hat{L_m}^2y^2\omega^2\left(y^2-1\right)}, & x\neq 1 \end{cases} \tag{11}$$

voltage. Therefore, to efficiently charge these two systems with the proposed module, the transformer turns ratio must be determined to allow the converter to operate around the resonant frequency while charging the battery at its nominal voltage. Another factor that can be determined is the M, which represents the ratio between the instantaneous charging voltage and the battery nominal voltage which can be represented as

$$M = \frac{V_{Char}(t)}{V_{battery-nominal}} \tag{13}$$

In Fig. 13, it can be noticed that almost all energy delivered to the battery is during $M > 0.9$. Consequently, the charging energy efficiency (η_e) is increased by delivering almost all the charging power at the unity gain operation point. Where η_e is defined as:

$$\eta_e = \frac{\int_0^T V_{in} I_{in}}{\int_0^T V_o I_o} \tag{14}$$

where T is the total charging time.

Therefore, the turns ratio (n) to charge the standard 400 V standard battery and the 800 V batteries while operating near the f_r is expressed as the follow:

$$n = \frac{V_{in}}{V_{battery-nominal}} \tag{15}$$

where the n is defined as $N_p : N_s$ of each transformer T_{r1} and T_{r2}, where N_p is the primary-side number of turns and N_s is the secondary-side number of turns.

The next step is to determine the transition point between the series and the parallel configurations that guarantees minimum resonant tank gain g deviation from unity gain in both configurations. The transition point which provides the minimum required (g) can be determined by

$$V_{transition} = \frac{2V_{in}}{n+1} \tag{16}$$

where $V_{transition}$ is the voltage point at which transition between the series and the parallel configurations occurs.

B. DETERMINE GAIN RANGE (g_{max} AND g_{min})

The required g in each configuration can be calculated to get the maximum and minimum gain. It should be noted that both configurations can achieve the same minimum and maximum gains, since they operate at the same quality factor Q_e. The maximum and the minimum gains can be determined as follows:

$$g_{\max} = \max\left\{\frac{nV_{\text{transition}}}{V_{in}}, \frac{V_{o-max}}{V_{in}}\right\} \tag{17}$$

$$g_{\min} = \min\left\{\frac{V_{\text{transition}}}{V_{in}}, \frac{nV_{o-\min}}{V_{in}}\right\} \tag{18}$$

Next, to realize the required gain, the LLC steady-state analytical model is used to determine the values of Q_e and L_n. Fig. 14 shows the converter circulating current against Q_e and L_n at fixed V_{in}, V_o, P_o, and f_r. By decreasing the Q_e and L_n, the circulating current is remarkably increased at the same output power. Moreover, in the boosting operation increasing the quality factor and inductance ratio to a certain point starts increasing the circulating current again. This happens because the converter capability to boost decreases, therefore the switching frequency significantly decreases and the circulating current passing through the magnetizing inductor increases. In conclusion, to reduce the circulating current the maximum Q_e and L_n that can achieve the required converter gain range has to be selected. Also, to be considered not increasing the Q_e and L_n to a point where the converter operates at very low switching frequency in boosting mode.

C. SELECT Q_e AND L_n

Before determining Q_e and L_n, two load resistances must be defined. The load resistance R_h at the highest gain and minimum load, and the load resistance R_l at the minimum gain and highest load. R_h and R_l can be calculated respectively as:

$$R_h = \frac{mV_{o-g_{\max}}^2}{P_{o-\max}} \tag{19}$$

$$R_l = \frac{mV_{o-g_{\min}}^2}{P_{o-\min}} \tag{20}$$

where m is substituted by the turns ratio in SM and twice the turns ratio in PM. From (5), (19), (20) and the fact that L_r and C_r are fixed for each design, the ratio between the quality factor (Q_{e-min}) at the minimum required gain and the quality factor (Q_{e-max}) at the maximum required gain can be defined as:

$$\frac{Q_{e-\min}}{Q_{e-\max}} = \frac{R_h}{R_l} = \zeta \tag{21}$$

The gain requirements are determined based on Q_e and L_n. The converter must achieve g_{max} at the load resistance (R_h,Q_{e-max}) and achieve g_{min} at the load resistance (R_l, Q_{e-min})

The Q_e and L_n can be defined using the maximum gain curves calculated by the LLC analytical model [28]. In Fig. 15, the converter g_{max}, and g_{min} are plotted against the converter parameters Q_e, and L_n. It can be seen that the bucking operation is mainly affected by Q_e. Hence, Q_e is selected based on the target g_{min}. The maximum Q_e is selected to reduce the reactive impedance and increase the power factor. The boosting region relies mainly L_n. Therefore, the maximum L_n is selected to achieve g_{max}, while avoiding high circulating current.

Then, to ensure ZVS operation, the turn-off current at minimum load and g_{min} should fulfill the following constrain:

$$I_{turnon} \geq \frac{4C_{oss}V_{in}}{t_{dead}} \tag{22}$$

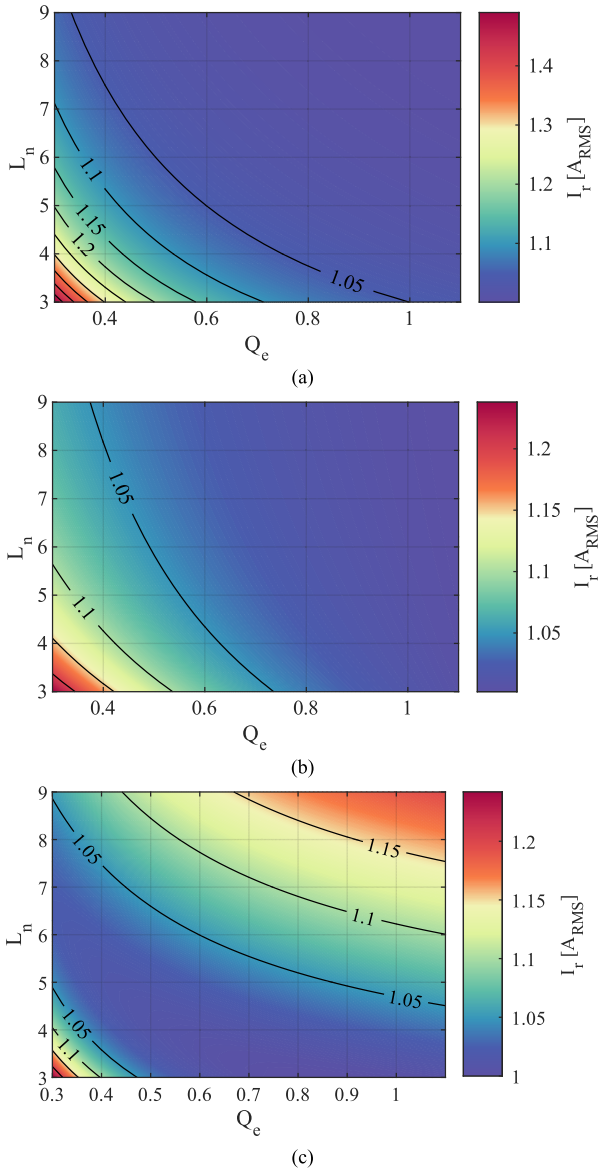

FIGURE 14. Resonant current ratio at constant P_o against Q_e and L_n based on time-domain analytical model (a) at $g = 1$ (b) at $g = 0.7$ (c) at $g = 1.3$.

where C_{oss} is the switch output capacitance, and t_{dead} is the dead time.

D. SELECT f_r AND CALCULATE L_r, C_r, AND L_m

Finally, the resonant frequency is determined by compromising between the power density and the switching losses. The resonant frequency selection is not included in this paper. Next, the converter resonant components values can be calculated as the following:

$$\begin{cases} C_r = \dfrac{1}{2\pi f_r Q_{e-\max} R_h} \\ L_r = (Q_{e-\max} R_h)^2 \cdot C_r \\ L_m = L_r \cdot L_n \end{cases} \tag{23}$$

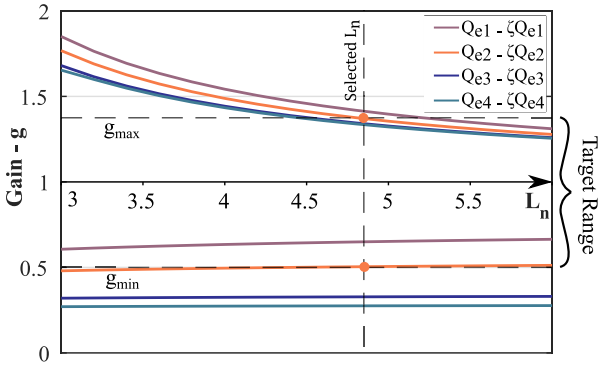

FIGURE 15. Converter gain characteristics based on time-domain analytical model.

TABLE 1. Module specification.

Parameters	Value
Input voltage (V_{in})	800 V
Output voltage (V_o)	200 - 1000 V
P_o / maximum I_o	10 kW / 36 A
L_r / C_r / L_m	42.5 µH/ 50 nF / 200 µH
Resonant Frequency (f_r)	120 kHz
Switching Frequency(f_{sw})	80 - 350 kHz
Transformer ratio (n)	2:1
Primary-side switch	Infineon SiC MOSFET IMZ120R045M1
Secondary-side diode	United SiC Schottky Diode UJ3D1250K2

IV. EXPERIMENTAL RESULTS

To verify the effectiveness of the proposed charging module, a 10 kW prototype converter is built and tested. The module performance is tested through the entire output voltage range of 200 - 1000 V with a 100 V increment. The module specification is shown in Table 1. The transformer is designed to have a low leakage inductance and it is measured to be less than $0.7\mu H$ using OMICRON Bode 100 spectrum analyzer. Therefore, the leakage inductance value is neglected compared to the resonant inductor and not considered in the analysis of the converter. A TI Delfino-F28379D DSP is used to control the converter and generate the driving signals. This experimental prototype is implemented under open loop control to validate the topology, design method, and provide proof of concept.

Fig. 19 shows the experimental setup. The converter waveforms in PM and SM at different operation points are shown in Fig. 16 and Fig. 17, respectively. Fig. 16 and Fig. 17 show the converter waveforms at the lowest gain operation at output voltage 200 V, maximum gain operation at output voltage 533 V, maximum voltage point (1000 V), and the unity gain operation at output voltage 400 V and 800V. These results are displayed by a Keysight DSOX2024A oscilloscope, Tektronix 5200A differential probe, and GMW CWT UM/03/B/1/80 current probe.

The primary H-bridge output voltage, the two transformers secondary voltages, and the resonant current is donated by V_{ab}, V_{s1}, V_{s2}, and I_r, respectively. In Fig. 16(c) and Fig. 17(c), there are oscillations in the secondary voltage

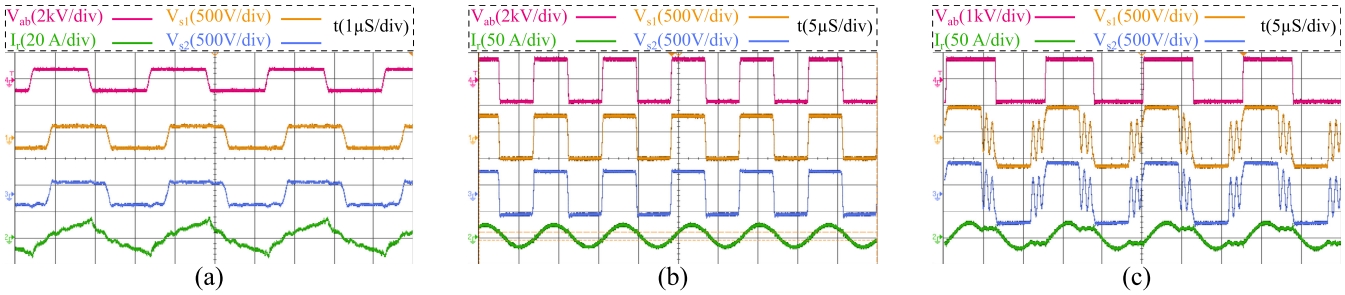

FIGURE 16. Experimental results of PM (a) 200 V, 2.5 kW, 337 kHz (b) 400 V, 10 kW, 120 kHz (c) 533 V, 10 kW, 85 kHz.

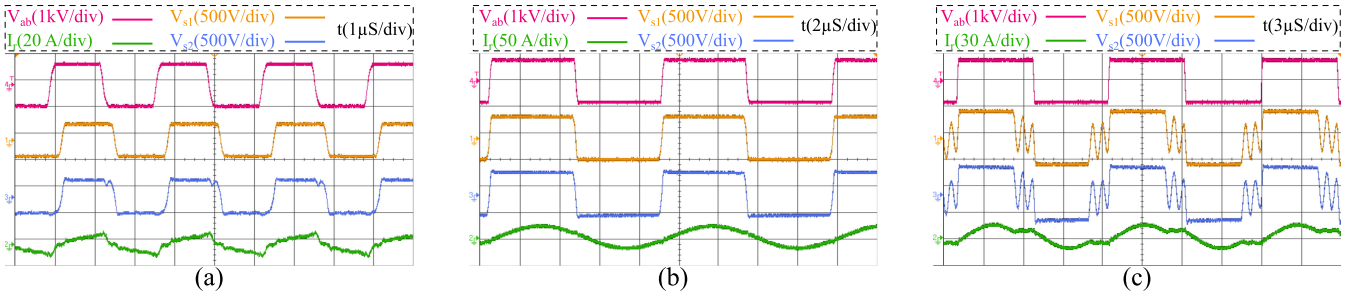

FIGURE 17. Experimental results of SM (a) 600 V, 2.5 kW, 215 kHz (b) 800 V, 10 kW, 120 kHz (c) 1000 V, 10 kW, 91 kHz.

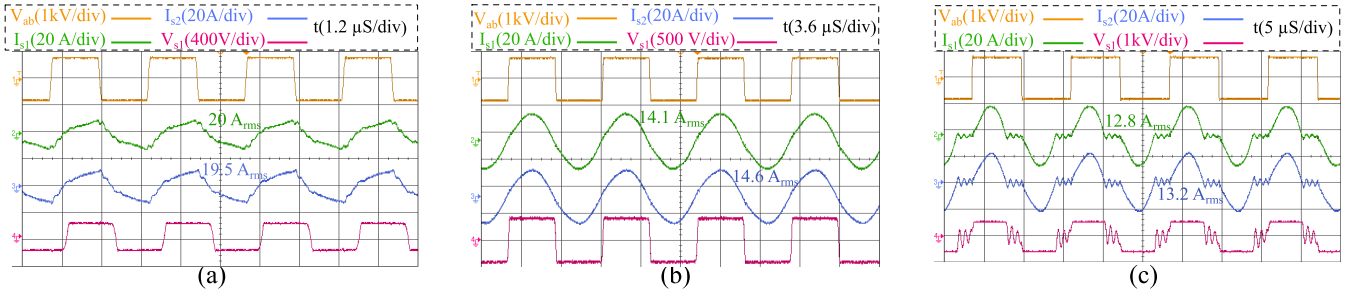

FIGURE 18. Secondary currents symmetry at PM at different voltage and power levels (a) 200 V, 2.5 kW, 215 kHz (b) 400 V, 10 kW, 120 kHz (c) 533 V, 10 kW, 85 kHz.

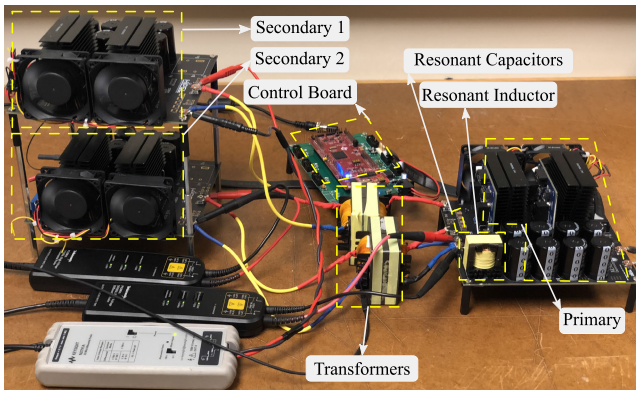

FIGURE 19. Experimental setup.

due to resonance between the circuit inductance and the transformer parasitic interwinding capacitance. This is a commonly seen phenomenon in the discontinuous current mode (DCM) in boosting operation.

The converter peak efficiency is around 98.7 % at an output voltage of 400 V. The converter efficiency is shown in Fig. 20. The converter is tested at the constant current (CC) region and the constant power (CP) region. The efficiency increases by increasing the output voltage and output power until reaching maximum efficiency at unity gain (400 V). Then, it drops to the transition voltage point due to deviating away from the resonant frequency. At the transition voltage (533 V), the secondaries reconfigure into SM. The efficiency elevates approaching the second unity gain operating point. To validate the two transformer secondaries current sharing, the two transformers secondary currents are shown and compared in 18, the two current measurements show identical waveforms and similar RMS with low measurement error. Additionally, the output current of each secondary at different voltage and power points are recorded in Table 2.

To evaluate the converter performance during the charging process the two 400 V and 800 V charging profiles shown in Fig. 13 were tested. The efficiency of the two charging

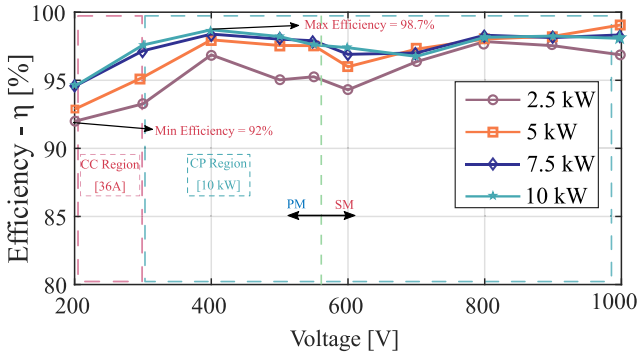

FIGURE 20. Measured experimental efficiency of the converter over the voltage range at different power levels.

TABLE 2. Current sharing error in pm.

V_o/P_{out} [V / kW]	$I_{o1}[A]$	$I_{o2}[A]$	Error-(ε) [%]
200/2.5	6	6.5	4
350/8	10.6	10.6	0
400/9.2	11.4	11.3	0.4
400/1.2	1.3	1.4	3.7

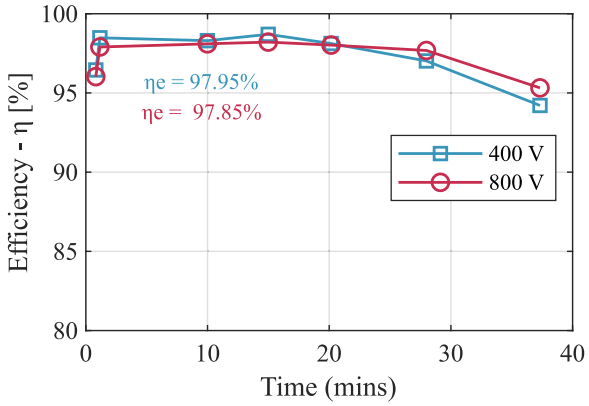

FIGURE 21. Experimental measured efficiency of 400 V and 800 V charging profiles.

profiles is shown in Fig. 21. The efficiency reaches 98.7 % and 98.2 % in the 400 V and the 800 V charging profiles, respectively. The η_e of the 400 V and the 800 V charging profiles is above 97.8 % as shown in Fig. 21. The lowest efficiency is around 94.2 % at low power operation at the charging profile end.It is important to highlight that the efficiency of low-power operation can be enhanced through the use of a multi-module charger. This is due to the fact that the output power of each module can be regulated in parallel with the other modules during high-power operation. During low-power operation, some of the modules can be deactivated, allowing the remaining modules to operate in a higher-power and, consequently, higher-efficiency region.

V. CONCLUSION

This paper proposes an LLC DC/DC charging module with configurable secondary for EV charging to extend the output voltage range of the converter without operating far from the resonant frequency. Additionally, this topology operates at the same Q_e during PM and SM, which simplifies the design process. Then, the converter design process is presented to achieve the required voltage and power range while minimizing the circulating current on the primary side. Finally, a 10 kW hardware prototype is developed and tested under different conditions for validation. The converter shows stable and efficient operation over the output voltage and load ranges with maximum efficiency of 98.5 %. The minimum efficiency recorded during typical charging is 94.2 %, which can be further increased in an actual charging station with several charging modules by controlling the power share between the modules.

REFERENCES

[1] IEA. (2021). *Global EV Outlook 2021*. Paris, France. [Online]. Available: https://www.iea.org/reports/global-ev-outlook-2021

[2] H. Tu, H. Feng, S. Srdic, and S. Lukic, "Extreme fast charging of electric vehicles: A technology overview," *IEEE Trans. Transport. Electrific.*, vol. 5, no. 4, pp. 861–878, Dec. 2019.

[3] M. R. Khalid, I. A. Khan, S. Hameed, M. S. J. Asghar, and J.-S. Ro, "A comprehensive review on structural topologies, power levels, energy storage systems, and standards for electric vehicle charging stations and their impacts on grid," *IEEE Access*, vol. 9, pp. 128069–128094, 2021.

[4] S. Ahmed et al., "Enabling fast charging—A battery technology gap assessment," *J. Power Sour.*, vol. 367, pp. 250–262, Nov. 2017.

[5] M. A. H. Rafi and J. Bauman, "A comprehensive review of DC fast-charging stations with energy storage: Architectures, power converters, and analysis," *IEEE Trans. Transport. Electrific.*, vol. 7, no. 2, pp. 345–368, Jun. 2021.

[6] D. Zhang, M. Guacci, M. Haider, D. Bortis, J. W. Kolar, and J. Everts, "Three-phase bidirectional buck-boost current DC-link EV battery charger featuring a wide output voltage range of 200 to 1000 V," in *Proc. IEEE Energy Convers. Congr. Expo.*, Oct. 2020, pp. 4555–4562.

[7] *UFC 200 Ultra Fast Charger*. Accessed: Apr. 19, 2022. [Online]. Available: https://www.deltaww.com/en-U.S./products/EV-Charging/5691/

[8] D. Cittanti, E. Vico, M. Gregorio, F. Mandrile, and R. Bojoi, "Iterative design of a 60 kW all-Si modular *LLC* converter for electric vehicle ultra-fast charging," in *Proc. AEIT Int. Conf. Electr. Electron. Technol. Automot.*, Nov. 2020, pp. 1–6.

[9] V. Monteiro, J. C. Ferreira, A. A. N. Melendez, C. Couto, and J. L. Afonso, "Experimental validation of a novel architecture based on a dual-stage converter for off-board fast battery chargers of electric vehicles," *IEEE Trans. Veh. Technol.*, vol. 67, no. 2, pp. 1000–1011, Feb. 2018.

[10] Z. Li, X. Yang, Y. Li, N. Wang, S. Zhang, H. Chen, and J. Ma, "A high-efficiency DC/DC converter with SiC devices and *LLC* topology for charging electric vehicles," in *Proc. Asian Conf. Energy, Power Transp. Electrific. (ACEPT)*, Oct. 2018, pp. 1–7.

[11] D. Zhang, M. Guacci, J. W. Kolar, and J. Everts, "Three-phase bidirectional ultra-wide output voltage range current DC-link AC/DC buck-boost converter," in *Proc. 46th Annu. Conf. IEEE Ind. Electron. Soc.*, 2020, pp. 4709–4716.

[12] V. M. Iyer, S. Gulur, G. Gohil, and S. Bhattacharya, "An approach towards extreme fast charging station power delivery for electric vehicles with partial power processing," *IEEE Trans. Ind. Electron.*, vol. 67, no. 10, pp. 8076–8087, Oct. 2020.

[13] J. Anzola, J. S. Artal-Sevil, I. Aizpuru, A. Arruti, R. Lopez, A. Alacano, and C. Bernal-Ruiz, "Resonant dual active bridge partial power converter for electric vehicle fast charging stations," in *Proc. IEEE Vehicle Power Propuls. Conf. (VPPC)*, Oct. 2021, pp. 1–6.

[14] N. D. Dao, D.-C. Lee, and Q. D. Phan, "High-efficiency SiC-based isolated three-port DC/DC converters for hybrid charging stations," *IEEE Trans. Power Electron.*, vol. 35, no. 10, pp. 10455–10465, Oct. 2020.

[15] W.-S. Lee, J.-H. Kim, J.-Y. Lee, and I.-O. Lee, "Design of an isolated DC/DC topology with high efficiency of over 97% for EV fast chargers," *IEEE Trans. Veh. Technol.*, vol. 68, no. 12, pp. 11725–11737, Dec. 2019.

[16] S. Deshmukh, A. Iqbal, S. Islam, I. Khan, M. Marzband, S. Rahman, and A. M. A. B. Al-Wahedi, "Review on classification of resonant converters for electric vehicle application," *Energy Rep.*, vol. 8, pp. 1091–1113, Nov. 2022.

[17] A. Jafari, M. S. Nikoo, F. Karakaya, and E. Matioli, "Enhanced DAB for efficiency preservation using adjustable-tap high-frequency transformer," *IEEE Trans. Power Electron.*, vol. 35, no. 7, pp. 6673–6677, Jul. 2020.
[18] S. Chaurasiya, N. Mishra, and B. Singh, "A 50 kW bidirectional fast EV charger with G2V V2G/V2V capability and wide voltage range," in *Proc. IEEE 5th Int. Conf. Comput. Commun. Autom. (ICCCA)*, Oct. 2020, pp. 652–657.
[19] Y. Xuan, X. Yang, W. Chen, T. Liu, and X. Hao, "A three-level dual-active-bridge converter with blocking capacitors for bidirectional electric vehicle charger," *IEEE Access*, vol. 7, pp. 173838–173847, 2019.
[20] H.-N. Vu and W. Choi, "A novel dual full-bridge *LLC* resonant converter for CC and CV charges of batteries for electric vehicles," *IEEE Trans. Ind. Electron.*, vol. 65, no. 3, pp. 2212–2225, Mar. 2018.
[21] X. Tang, Y. Xing, H. Wu, and J. Zhao, "An improved *LLC* resonant converter with reconfigurable hybrid voltage multiplier and PWM-plus-PFM hybrid control for wide output range applications," *IEEE Trans. Power Electron.*, vol. 35, no. 1, pp. 185–197, Jan. 2020.
[22] M. Safayatullah, M. T. Elrais, S. Ghosh, R. Rezaii, and I. Batarseh, "A comprehensive review of power converter topologies and control methods for electric vehicle fast charging applications," *IEEE Access*, vol. 10, pp. 40753–40793, 2022.
[23] N. Zanatta, T. Caldognetto, D. Biadene, G. Spiazzi, and P. Mattavelli, "Design and implementation of a two-stage resonant converter for wide output range operation," *IEEE Trans. Ind. Appl.*, vol. 58, no. 6, pp. 7457–7468, Nov. 2022.
[24] A. Awasthi, S. Bagawade, and P. K. Jain, "Analysis of a hybrid variable-frequency-duty-cycle-modulated low-*Q* *LLC* resonant converter for improving the light-load efficiency for a wide input voltage range," *IEEE Trans. Power Electron.*, vol. 36, no. 7, pp. 8476–8493, Jul. 2021.
[25] L. Shi, B. Liu, and S. Duan, "Burst-mode and phase-shift hybrid control method of *LLC* converters for wide output range applications," *IEEE Trans. Ind. Electron.*, vol. 67, no. 2, pp. 1013–1023, Feb. 2020.
[26] J. Baek, K.-W. Kim, H.-S. Youn, and C.-E. Kim, "High-efficiency *LLC* resonant converter with reconfigurable voltage multiplying rectifier for wide output voltage applications," *IEEE Trans. Power Electron.*, vol. 36, no. 7, pp. 7641–7651, Jul. 2021.
[27] Y. Zuo, X. Pan, and C. Wang, "A reconfigurable bidirectional isolated *LLC* resonant converter for ultra-wide voltage-gain range applications," *IEEE Trans. Ind. Electron.*, vol. 69, no. 6, pp. 5713–5723, Jun. 2022.
[28] Z. Fang, T. Cai, S. Duan, and C. Chen, "Optimal design methodology for *LLC* resonant converter in battery charging applications based on time-weighted average efficiency," *IEEE Trans. Power Electron.*, vol. 30, no. 10, pp. 5469–5483, Oct. 2015.
[29] W. Guo, K. Bai, A. Taylor, J. Patterson, and J. Kane, "A novel soft starting strategy of an *LLC* resonant DC/DC converter for plug-in hybrid electric vehicles," in *Proc. 28th Annu. IEEE Appl. Power Electron. Conf. Expo. (APEC)*, Mar. 2013, pp. 2012–2015.
[30] H. Wang, Y. Chen, Y.-F. Liu, J. Afsharian, and Z. A. Yang, "A common inductor multi-phase *LLC* resonant converter," in *Proc. IEEE Energy Convers. Congr. Expo. (ECCE)*, Sep. 2015, pp. 548–555.
[31] Z. Hu, L. Wang, H. Wang, Y.-F. Liu, and P. C. Sen, "An accurate design algorithm for *LLC* resonant converters—Part I," *IEEE Trans. Power Electron.*, vol. 31, no. 8, pp. 5435–5447, Aug. 2016.
[32] *Electric Vehicle Conductive Charging System—Part 1: General Requirements*, Standard EN IEC 61851-1, 2019.
[33] Idaho National Lab. *DC Fast Charger Fact Sheet: ABB Terra 53 CJ Charging a 2015 Nissan Leaf*. Accessed: May 5, 2022. [Online]. Available: https://avt.inl.gov/

AHMED ELEZAB (Student Member, IEEE) received the B.S. degree in mechatronics engineering from Ain Shams University, Cairo, Egypt, in 2019. He is currently pursuing the Ph.D. degree with McMaster University, Hamilton, ON, Canada. During his undergraduate studies, he participated in Shelleco Marathon Competition for EVs as an Electric Powertrain Member. He has been a part of the HiPEL Research Group, since May 2020. His research interests include developing ultrafast battery chargers for electrified vehicles and the development of multilevel high-power industrial-grade motor drive systems.

OMAR ZAYED (Graduate Student Member, IEEE) received the B.Sc. degree in mechatronics engineering from Ain Shams University, Egypt, in 2019, and the M.Sc. degree from the Electrical and Computer Engineering Department, McMaster University, Hamilton, ON, Canada, where he is currently pursuing the Ph.D. degree, with a focus on the design and development of power electronic converters. He is currently working on ultrafast chargers for EVs with the High-Power Electronics Laboratory (HiPEL), McMaster University. His research interests include power electronics converters and medium-voltage motor drives for industrial applications.

AHMED ABUELNAGA (Member, IEEE) received the B.Sc. (Hons.) and M.Sc. degrees in electrical engineering from Ain Shams University, Cairo, Egypt, in 2012 and 2017, respectively, and the Ph.D. degree from the Department of Electrical and Computer Engineering, McMaster University, Hamilton, ON, Canada, in 2021. From 2012 to 2017, he was a Teaching Staff with the Department of Electrical Power and Machines, Ain Shams University. Since 2018, he has been working on research and development with Rockwell Automation, Cambridge, ON, Canada. Since 2018, he has been working on research and development with Rockwell Automation, Cambridge, ON, Canada. His research interests include power electronics interfaces, motor drives, embedded control, reliability, and predictive maintenance.

MEHDI NARIMANI (Senior Member, IEEE) received the Ph.D. degree in electrical engineering from the University of Western Ontario, London, ON, Canada, in 2012. He is currently an Associate Professor with the Department of Electrical and Computer Engineering and the University Scholar with McMaster University, Hamilton, ON, Canada. He also holds the NSERC Canada Research Chair (CRC) position in high-power converter systems. Before joining McMaster University, he was a Power Electronics Engineer with Rockwell Automation Canada, Cambridge, ON, Canada. He has authored/coauthored more than 150 journal and conference proceeding papers, coauthored a Wiley-IEEE Press book, and holds eight issued/pending U.S./European patents. His current research interests include power conversion, the control of power electronics converters, fast EV chargers, and wireless EV charging systems. He has been an Associate Editor for IEEE TRANSACTIONS ON POWER ELECTRONICS and IEEE TRANSACTIONS ON VEHICULAR TECHNOLOGY and the Vice Chair and the Topic Chair of top-tier conferences, such as IEEE Energy Conversion Congress and Exposition (IEEE ECCE) and IEEE Applied Power Electronics Conference and Exhibition (IEEE APEC).